

Defect-annealing-induced optical gain recovery in electron-irradiated 4H-SiC UV phototransistors

Cite as: Appl. Phys. Lett. **127**, 103302 (2025); doi: [10.1063/5.0287853](https://doi.org/10.1063/5.0287853)

Submitted: 27 June 2025 · Accepted: 21 August 2025 ·

Published Online: 10 September 2025



Qunsi Yang,^{1,2} Yifu Wang,³ Xinghua Liu,⁴ Qianyu Hou,⁵ Lihui Song,^{1,2,a} Hai Lu,³ Deren Yang,^{1,2} and Xiaodong Pi^{1,2,a}

AFFILIATIONS

¹State Key Laboratory of Silicon and Advanced Semiconductor Materials & School of Materials Science and Engineering, Zhejiang University, Hangzhou 310027, China

²Key Laboratory of Power Semiconductor Materials and Devices of Zhejiang Province & Institute of Advanced Semiconductors, ZJU-Hangzhou Global Scientific and Technological Innovation Center, Zhejiang University, Hangzhou 311200, China

³Collaborative Innovation Center of Advanced Microstructures, School of Electronic Science and Engineering, Nanjing University, Nanjing 210093, China

⁴Jiangsu Province Engineering Research Center of Photonic Devices and System Integration for Communication Sensing Convergence, School of Electronic Information and Engineering, Wuxi University, Wuxi 214105, China

⁵School of Physical Science and Technology, Guangxi University, Nanning 530004, China

^aAuthors to whom correspondence should be addressed: songlihui@zju.edu.cn and xdpi@zju.edu.cn

ABSTRACT

The ultraviolet (UV) response of a floating-base 4H-SiC n-p-n phototransistor is characterized before and after 10 MeV electron irradiation. The pristine device demonstrates visible-blind UV detection at 275 nm, achieving a UV/dark current ratio of $\sim 10^6$, a specific detectivity of 1.37×10^{12} Jones, and a responsivity of 1.36 A/W. Responsivity monotonically increases with incident optical power density. After 500 kGy irradiation, responsivity degrades by 80%, with dose dependence following a double-exponential decay. Vacuum annealing at 800 K restores 79% of the pre-irradiation optical gain, confirming a partial reversibility of irradiation-induced defects. Deep level transient spectroscopy reveals defect evolution post-annealing, identifying corresponding energy levels, identities, and annihilation dynamics. High-temperature annealing primarily annihilates irradiation-induced point defects, enabling significant recovery, while thermally stable defect complexes prevent full restoration.

Published under an exclusive license by AIP Publishing. <https://doi.org/10.1063/5.0287853>

Wide bandgap semiconductors, particularly silicon carbide (4H-SiC), have emerged as pivotal materials for ultraviolet (UV) detection in extreme environments due to their inherent advantages, including high thermal conductivity, intrinsic visible blindness, and exceptional radiation tolerance.^{1–3} These properties enable 4H-SiC-based detectors to operate reliably in harsh conditions, such as space radiation environments, nuclear facilities, and high-temperature industrial processes, where conventional silicon-based devices typically fail.^{4,5} Significant progress has been made over the past decade in developing 4H-SiC UV detectors, with architectures ranging from simple photodiodes (e.g., p-n diode,⁶ p-i-n diode,^{7,8} and Schottky barrier diode^{9,10}) to advanced avalanche photodiodes (APDs).^{11,12} However, achieving high internal gain in these devices often compromises response speed or noise performance. To address this limitation, bipolar junction phototransistors (BJPTs) have gained attention for their

inherent current amplification capability, which combines high sensitivity with fast response. The n-p-n configuration featuring a floating base is particularly promising for solar-blind UV detection, offering high responsivity, low output noise, and streamlined processing compatibility.^{13–15}

Despite these advancements, the radiation hardness of 4H-SiC phototransistors—a critical requirement for space and nuclear applications—remains insufficiently characterized. While 4H-SiC exhibits superior displacement damage resistance compared to silicon, high-energy particle irradiation can still induce point defects (e.g., carbon vacancies and silicon interstitials) and defect complexes. These defects degrade optoelectronic performance primarily through carrier trapping and Shockley-Read-Hall (SRH) recombination. Previous studies have predominantly focused on the effects of proton,^{16,17} gamma-ray,¹⁸ or neutron irradiation¹⁹ on commercially utilized 4H-

SiC power devices, particularly analyzing displacement damage and total ionizing dose (TID) effects. Nevertheless, information regarding the impact of high-energy electron irradiation—a dominant component of geostationary orbit radiation—on the UV detection performance of 4H-SiC phototransistors is currently very scarce.

The low mass of electrons preferentially induces inelastic collisions, strongly suppressing atomic displacements while enhancing ionization effects. Although high-energy electrons can generate isolated point defects through cumulative lattice vibrations that locally exceed displacement thresholds, their primary damage mechanism remains ionization-dominated. This leads to metastable defects with unique thermal recovery pathways, contrasting sharply with the stable defect clusters produced by proton irradiation through direct displacement cascades. These irradiation-induced variations in the device's electrical characteristics pose a dramatic challenge for predictive modeling of its long-term reliability in radiation-rich environments, especially during extended missions, where cumulative dose effects lead to nonlinear performance degradation.

This work quantitatively evaluates the impact of 10-MeV electron irradiation on the UV detection performance of floating-base 4H-SiC n-p-n phototransistors. The study focuses on three critical aspects: (1) intrinsic performance analysis: characterizing the device's inherent UV detection performance, with emphasis on the current amplification capability and the related energy band modulation under dark and UV illuminated conditions; (2) dose-response correlation: quantifying the relationship between responsivity degradation and ionizing dose, identifying dose-dependent carrier trapping and recombination pathways governing the optoelectronic performance degradation; and (3) defect characterization and annealing: identifying the energy levels and possible identities of irradiation-induced defects using DLTS, before and after 800-K annealing, to reveal defect annihilation and structural reconfiguration processes.

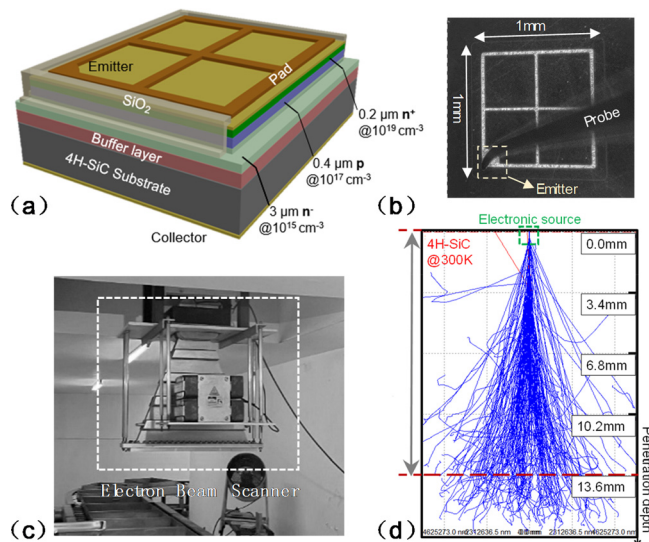


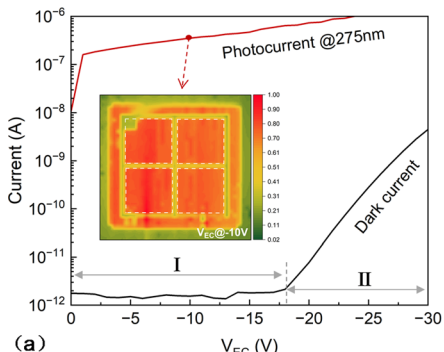
FIG. 1. (a) Schematic cross section diagram of the floating-base 4H-SiC n-p-n phototransistor. (b) The photograph of the fabricated device. (c) High-energy electron linear accelerator in Zhejiang University. (d) Incident trajectory of 10-MeV electrons in 4H-SiC simulated by the Casino program.

The floating-base 4H-SiC n-p-n phototransistor architecture is shown in Fig. 1(a). The epitaxial structure grown on a 4-in. n^+ -type 4H-SiC substrate consists of three key functional layers: a 3.0- μm -thick n -type collector layer (doping conc. $\sim 1 \times 10^{15} \text{ cm}^{-3}$), a 0.4- μm -thick p -type base layer (doping conc. $\sim 1 \times 10^{17} \text{ cm}^{-3}$), and a 0.2- μm -thick heavily doped n^+ -emitter layer (doping conc. $\sim 1 \times 10^{19} \text{ cm}^{-3}$). Device fabrication is initiated with mesa etching through the emitter and base layers using inductively coupled plasma (ICP) etching with SF_6/O_2 gas mixture, exposing the collector layer. Subsequent thermal oxidation at 1050°C for 60 min in dry O_2 served to repair plasma-induced lattice defects.²⁰ A 500-nm-thick SiO_2 passivation layer is subsequently deposited using plasma-enhanced chemical vapor deposition (PECVD). Contact windows are patterned using buffered oxide etchant (BOE) wet chemical etching, followed by the deposition of Ni/Ti/Al/Au (35/50/100/100 nm) multilayer metal stacks via electron beam evaporation (EBE) to serve as the emitter and collector electrodes. Subsequent rapid thermal annealing (RTA) at 850°C for 3 min in N_2 ambient is carried out to form Ohmic contacts. Final front Ni/Au (500/500 nm) contact pads are deposited using magnetron sputtering. The completed device demonstrates a compact $1.0 \times 1.0 \text{ mm}^2$ active area, as confirmed by the optical micrograph in Fig. 1(b).

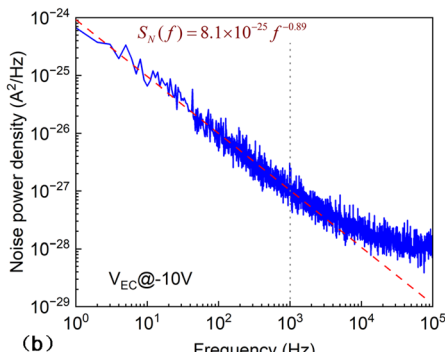
Figure 1(c) demonstrates that the high-energy electron irradiation experiments are conducted at ambient temperature utilizing an electron linear accelerator CIAE-FZ-10/15 from the Institute of Nuclear Agricultural Sciences at Zhejiang University. A collimated 10-MeV electron beam (dose range 1–500 kGy) is aimed perpendicularly at the surface of the phototransistor. As shown in Fig. 1(d), the Casino calculation shows that the penetration depth of 10-MeV electrons in 4H-SiC easily exceeds 13.6 mm, significantly surpassing the whole epitaxial layer and substrate as well, leading to complete beam transmission and nearly uniform defect generation along the trajectory. The cumulative ionizing dose is calibrated using a dichromate dosimeter, co-located with the unbiased device within the irradiation chamber. Intermittent electrical characterizations are measured during beam-off intervals and compared with those obtained on the pristine device.

Phototransistors typically operate in the forward-active mode, where the emitter-base (E-B) junction is forward-biased and the base-collector (B-C) junction remains reverse-biased to enable controlled carrier amplification. As shown in Fig. 2(a), under 275 nm UV illumination, the photocurrent of the 4H-SiC n-p-n phototransistor exhibits a pronounced contrast with the dark current. The device displays a UV-to-dark current ratio ($I_{\text{ph}}/I_{\text{dark}}$) roughly reaching 10^6 at an emitter-collector voltage (V_{EC}) of -10 V, demonstrating superior UV sensitivity and effective dark current suppression. As can be seen, the device shows an extremely low dark current of $\sim 1 \text{ pA}$ over the V_{EC} range of 0 to -17 V (marked as region I) and then increases exponentially (marked as region II). The device exhibits distinct operational regimes governed by the applied bias V_{EC} .

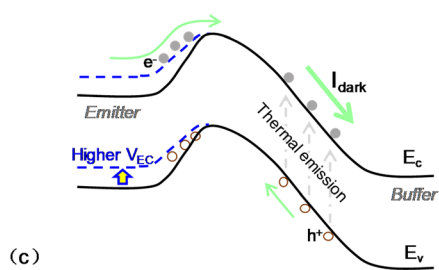
In region I, characteristic bipolar transistor cutoff behavior dominates, with a reverse leakage current of $\sim 2 \text{ pA}$ comparable to the conventional 4H-SiC p-i-n UV detector, confirming thermionic emission across the reverse-biased B-C junction as the primary carrier transport mechanism. Beyond the punch-through threshold voltage (V_{PT}), lateral expansion of the collector depletion region induces spatial coupling with the E-B junction depletion zone. This coupling simultaneously reduces the E-B junction conduction band barrier through electrostatic superposition and enhances electron injection



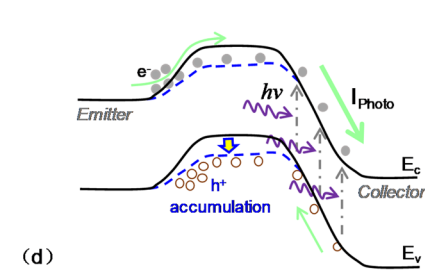
(a)



(b)



(c)



(d)

FIG. 2. (a) The dark current and photocurrent of the 4H-SiC n-p-n phototransistor. Inset: normalized photocurrent mapping profiles. (b) Noise power spectral density measured in the dark. Energy band diagram depicting: (c) dark current surge at $V_{EC} > V_{PT}$, with dashed blue line showing band shift with higher V_{EC} . (d) photocurrent gain at $V_{EC} < V_{PT}$, with dashed blue line indicating band bending from photo-induced holes.

from the emitter. Consequently, the collector current escalates by 3 orders of magnitude, from 2 pA at -17 V to 5 nA at -30 V . This abrupt transition aligns well with the punch-through transport characteristic,²¹ where sub-picosecond carrier transit time enables direct field-driven injection. The energy band evolution underlying these mechanisms is systematically resolved in Fig. 2(c), corroborating the interplay between depletion geometry and barrier modulation. The above-mentioned results indicate that the phototransistors fabricated in this work are suitable for an operating voltage range of 0 to -17 V . All subsequent measurements are performed with the device's V_{EC} kept at -10 V under steady-state operating conditions. A focused 266 nm UV laser beam (spot diameter: $4\text{ }\mu\text{m}$) is raster-scanned across the device surface with simultaneous photocurrent mapping. As presented in the inset of Fig. 2(a), the normalized photocurrent distribution reveals an RMS inhomogeneity of less than 10% within the device's photosensitive region, reflecting the uniformity of the doping concentration and the consistency of the defect density distribution in the epitaxial layer.

The specific detectivity (D^*), a critical figure of merit for photodetectors, is rigorously evaluated for the phototransistor through noise characterization. As detailed in Fig. 2(b), the noise power spectral density (S_N) is acquired under dark conditions using a low-noise current preamplifier (SR570) coupled with a fast Fourier transform spectrum analyzer (SR785). The measured noise spectrum exhibits two distinct regimes: below 1 kHz, the data follow an $S_N(f) \propto f^A$ dependence characteristic of dominant flicker noise, as confirmed by SPICE model fitting; above 1 kHz, S_N stabilizes near the instrument-limited floor of $10^{-28}\text{ A}^2/\text{Hz}$. These measurements enabled the calculation of the noise equivalent power (NEP) and normalized D^* by using the following equations, respectively,

$$NEP = \sqrt{\int_0^B S_N(f) df} / R, \quad (1)$$

$$D^* = \sqrt{A \times BW} / NEP, \quad (2)$$

where R is the responsivity, A is the active area of the device, and BW is the operational bandwidth. At 275 nm illumination, the NEP reaches 1.84 pW with corresponding D^* of 1.37×10^{12} Jones, demonstrating its capability for weak UV signal detection under reverse bias operation.²²

Figure 3 shows the wavelength and light intensity-dependent responsivity of the 4H-SiC phototransistor under reverse bias of -10 V . Under 275 nm UV illumination, the responsivity increases with incident optical power density, achieving 1.36 A/W at 1.07 mW/cm^2 , confirming the presence of an intrinsic gain

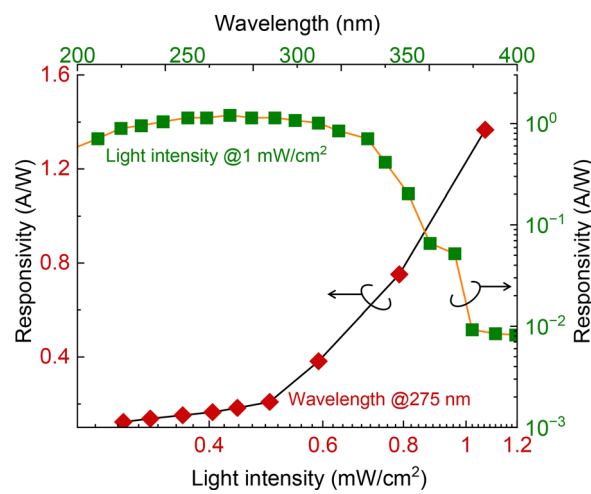


FIG. 3. Responsivity as a function of incident UV light intensity (left axis) and wavelength (right axis) measured at the bias of -10 V .

mechanism. The responsivity comparison presented in [supplementary material](#) Fig. S5 demonstrates the device's potential for highly sensitive UV detection. At a fixed light intensity of 1 mW/cm^2 , the spectral response peaks at $\sim 275 \text{ nm}$, with a UV-to-visible (275–400 nm) rejection ratio exceeding 100. The photocurrent amplification originates from the carrier transport dynamics inherent to the n-p-n architecture, as depicted in [Fig. 2\(d\)](#). Photogenerated holes within the B-C depleted zone are driven toward the base region by the applied electric field, leading to their accumulation at the E-B junction interface. This charge accumulation induces pronounced band bending, effectively lowering the junction potential barrier. Consequently, emitter electrons overcome the barrier and inject into the base region, contributing an I_{ph} component to the collector current.

[Figure 4\(a\)](#) shows the dark current and photocurrent of the 4H-SiC phototransistor irradiated upon various electron doses. The dark current of the irradiated device in the cutoff regime remains nearly unchanged for doses up to 500 kGy, corresponding to an electron fluence of $1.75 \times 10^{15} \text{ cm}^{-2}$. At the same time, the V_{PT} increases from 17 to 26 V after 1-kGy irradiation, while the leakage current at the bias of -26 V decreases by 3 orders of magnitude. This behavior aligns well with the prior reports on the radiation-induced conductivity degradation attributed to the removal of free carriers via deep trap states introduced by high-energy particle irradiation.²³ The photocurrent exhibits a monotonic decrease as a function of cumulative radiation dose. A rapid photocurrent degradation is observed below a dose of 200 kGy, followed by a slower attenuation rate at higher doses. Notably, the device maintains an $I_{\text{ph}}/I_{\text{dark}}$ ratio of $\sim 10^6$ even after 500-kGy irradiation, demonstrating exceptional radiation tolerance suitable for harsh radiative environments.

The radiation-induced degradation of responsivity under electron irradiation is characterized in [Fig. 4\(b\)](#). The normalized responsivity exhibits a rapid decrease of 70% before reaching an irradiation dose of 20 kGy, followed by a significantly attenuated decline rate at higher doses, ultimately approaching saturation. This dual-phase degradation behavior is accurately described by a double-exponential decay function, previously employed to model proton irradiation-induced degradation in polycrystalline diamond detectors.²⁴ The equation comprises two exponential terms with distinct dose constants,

$$R(D) = 1 - p_1(1 - e^{-\frac{D}{D_1}}) - p_2(1 - e^{-\frac{D}{D_2}}), \quad (3)$$

where D denotes the irradiation dose, p_1 and p_2 represent the relative contributions of defect-mediated recombination losses attributed to

simple defects and complex cluster-related defects, respectively. Here, D_1 and D_2 correspond to critical doses at which simple defects and cluster-related defects dominate the responsivity degradation. Detailed fitting results are provided in [supplementary material](#) Fig. S6. During initial irradiation, high-energy electrons interact with lattice atoms to generate isolated point defects (e.g., single interstitials and monovacancies). These defects act as both carrier traps and recombination centers, significantly inducing carrier compensation while reducing photogenerated carrier density. Crucially, the carrier compensation effect dominates responsivity degradation, as increasing radiation dose should enhance carrier recombination; the responsivity degradation does not accelerate progressively but instead nearly saturates beyond 20 kGy irradiation, indicating the initial responsivity degradation is indeed dominated by the carrier compensation effect. With increasing irradiation dose, cumulative displacement damage facilitates the progressive accumulation of deep-level defects and the formation of defect complexes. These extended defects degrade carrier mobility through enhanced scattering mechanisms and suppress carrier collection efficiency due to localized potential barriers and non-radiative (mainly SRH) recombination pathways. Beyond 20 kGy irradiation, saturation of the carrier compensation effect attenuates responsivity degradation. After 500-kGy irradiation, the device retains 20% of its initial performance, demonstrating the significant influence of large dose electron irradiation on the device performance.

The optical gain (G), a critical parameter governing optoelectronic performance,¹³ is systematically evaluated under three distinct operational states: pre-irradiation, post-500-kGy electron irradiation, and post-irradiation annealing at 800 K. The gain is defined as

$$G = \Delta I_{\text{C}} h\nu / (\eta q P_{\text{in}}), \quad (4)$$

where $\Delta I_{\text{C}} = I_{\text{ph}} - I_{\text{dark}}$ is the net collector photocurrent, $h\nu$ is the incident photon energy, η is the external quantum efficiency (EQE), and P_{in} is the incident optical power. As shown in [Fig. 5\(a\)](#), the optical gain exhibits a monotonic increase with optical power density, consistent with the trend of responsivity as mentioned above. The gain significantly decreases after irradiation, showing a 66% reduction at $\sim 1.0 \text{ mW/cm}^2$ light power. Following a vacuum annealing process at 800 K for 5 min, a partial recovery of optical gain is observed, reaching 79% of its initial performance. [Supplementary material](#) Fig. S7 confirms the voltage-independent nature of the gain recovery rate. This outcome signifies that most thermally unstable, irradiation-induced defects can be efficiently annealed out at 800 K.

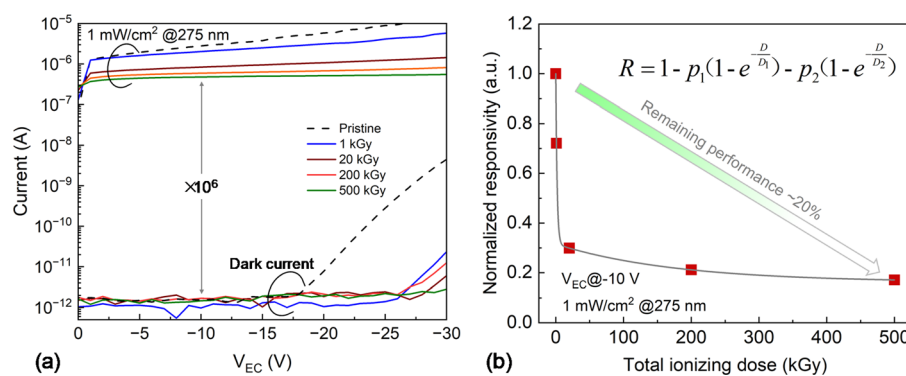


FIG. 4. (a) The dark current and photocurrent measured before and after electron irradiation. (b) Effect of the various total ionizing doses on the normalized responsivity.

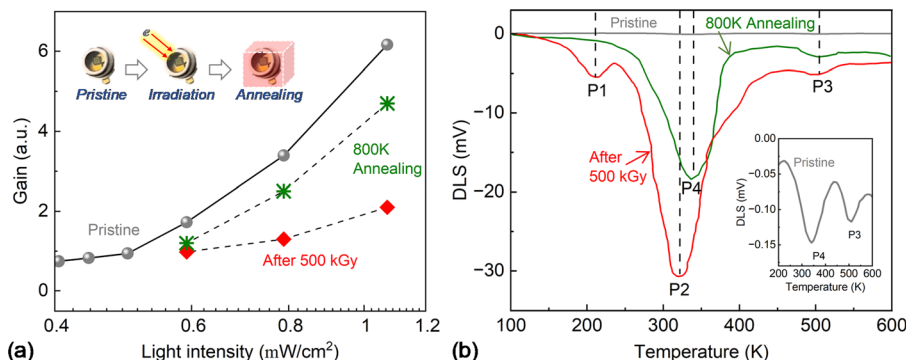


FIG. 5. State-dependent characteristics: (a) Optical gain as a function of incident light intensity; (b) DLTS spectra of 4H-SiC p-n diode. Both measured in three states: pristine, 500 kGy electron-irradiated, and 800 K annealed post-irradiation. Inset: enlarged view of the DLTS spectrum at pristine state.

DLTS measurements probe defect evolution dynamics in a p-n junction device that electrically emulates the B-C junction of the phototransistor. Identical irradiation/annealing protocols ensure defect generation and recovery processes remain directly comparable. This study selectively probes defects in the collector for two reasons. First, electron traps in the *p*-type base produce negligible DLTS signals due to majority carrier masking, whereas their signatures become resolvable in the *n*-type collector. Second, the low electron interaction cross section ensures uniform damage distribution across the device depth, making the collector a representative defect-analysis region. Thus, collector-derived DLTS data effectively elucidate electron trap formation mechanisms in the base.

As shown in Fig. 5(b), the DLTS spectrum recorded after 500-kGy irradiation reveals three prominent defect-related peaks labeled as P1 (212 K), P2 (320 K), and P3 (504 K). Negative DLTS peaks evidence electron trapping at majority carrier defects in *n*-type 4H-SiC. Hence, the *n*-type epilayer (emitter/collector regions) becomes compensated even at low irradiation doses, inducing pronounced V_{PT} advancement at doses as low as 1 kGy. Post-annealing at 800 K induces substantial defect recovery, characterized by nearly complete elimination of the P1 peak and significant intensity reduction of P2 and P3. Notably, the P2 peak shifts to higher temperatures and narrows, with its peak position converging to that of the P4 peak in the pristine sample. The P2 peak decomposition suggests two overlapping defects: a primary defect can be annealed out at 800 K and a thermally stable counterpart inhibits post-annealing performance restoration.

Table I summarizes defect parameters (the energy position E_C-E_T related to the conduction band edge, the electron capture cross section σ_n , and concentration N_t) and proposed identities. The detected traps P1–P4 exhibit energy levels at $E_C-0.32$ eV, $E_C-0.57$ eV, $E_C-1.02$ eV, and

$E_C-0.63$ eV, respectively. Their σ_n match established signatures of E_1 , E_2 , EH_4 , and $Z_{1/2}$ centers. Annealing drives substantial defect transformation in 4H-SiC, completely eliminating E_1 centers (DLTS-undetectable) while reducing E_2 -family defects to $Z_{1/2}$ configurations and lowering EH_4 center concentration by 65%. It has been reported that the metastable E_1 center originates from carbon interstitials (C_i),²⁵ while the deep-level EH_4 corresponds to an irradiation-induced extended defect complex.²⁶ The $Z_{1/2}$ center—a double negative acceptor state—is assigned to carbon vacancies (V_C) at hexagonal/pseudo-cubic lattice sites,^{27–29} strongly anchored to the lattice, being stable up to 1500 °C.^{30,31} After post-annealing, the $Z_{1/2}$ defect dominates the DLTS spectrum as a carrier lifetime killer, accompanied by the deep-level EH_4 cluster. The limited atomic displacements from electron irradiation nevertheless permit gradual defect accumulation through an ionization-mediated process. As irradiation dose progresses, the sustained generation of electron-hole pairs activates defect migration pathways, enabling initially isolated point defects to evolve into stable defect complex configurations. Simple defects and radiation-stabilized complexes act synergistically to drive carrier compensation and recombination losses, evidenced by double-exponential responsivity decay. Although annealing removes metastable defects to enable significant recovery, residual defect complexes impose intrinsic restoration limits.

This study provides a comprehensive analysis of the irradiation effects of 10-MeV electrons on the performance of floating-base 4H-SiC n-p-n phototransistor. Electro-optical test results verify the phototransistor's current amplification feature and good UV detection performance. The degradation behavior of responsivity with increasing dose aligns well with a double-exponential decay model, suggesting the presence of irradiation dose-dependent competing mechanisms for defect evolution. Thermal annealing significantly restores the performance of the irradiated device, highlighting the dynamic reversibility of radiation-induced defects. The DLTS analysis further reveals the evolutionary mechanism of high-temperature annealing on irradiation-induced defects, i.e., thermally unstable defects undergo annihilation or transition to stable configurations. These findings provide fundamental guidelines for designing radiation-hardened wide-bandgap photonic devices targeting extreme environments in aerospace systems and nuclear facilities.

TABLE I. The energy position, E_a , capture cross section, σ_n , concentration, N_t , and possible identity for different traps observed by DLTS measurements.

Peak	E_a (eV)	σ_n (cm ²)	N_t (cm ⁻³)	Identity
P1	$E_C-0.32$	5×10^{-13}	6.2×10^{13}	E_1
P2	$E_C-0.57$	5×10^{-14}	4.3×10^{14}	E_2
P3	$E_C-1.02$	2×10^{-13}	$5.7 \times 10^{13} / 2.0 \times 10^{13}$ ^a	EH_4
P4	$E_C-0.63$	6×10^{-14}	6.2×10^{13}	$Z_{1/2}$

^aConcentration N_t of EH_4 and $Z_{1/2}$ after 800 K annealing.

See the [supplementary material](#) for detailed information on the photocurrent mapping and DLTS characterization, high-temperature current-voltage characteristics, responsivity benchmarking against various 4H-SiC UV detector architectures, double-exponential decay function fitting results, and bias-dependent gain recovery analysis.

This work was supported by the Innovation Program for Quantum Science and Technology (No. 2021ZD0303400), the National Natural Science Foundation of China (Nos. 12303100, U2141241, U21A20496, and 62374084), and the Zhejiang Provincial Natural Science Foundation of China (No. LMS25F040003).

AUTHOR DECLARATIONS

Conflict of Interest

The authors have no conflicts to disclose.

Author Contributions

Qunsi Yang: Data curation (equal); Formal analysis (equal); Investigation (equal); Methodology (equal); Visualization (equal); Writing – original draft (lead); Writing – review & editing (equal). **Yifu Wang:** Methodology (equal); Visualization (equal). **Xinghua Liu:** Data curation (supporting); Methodology (supporting). **Qianyu Hou:** Formal analysis (supporting); Methodology (supporting). **Lihui Song:** Data curation (equal); Formal analysis (equal); Funding acquisition (equal); Investigation (equal); Writing – review & editing (equal). **Hai Lu:** Conceptualization (equal); Resources (equal); Supervision (equal). **Deren Yang:** Resources (equal); Supervision (equal). **Xiaodong Pi:** Conceptualization (equal); Formal analysis (equal); Funding acquisition (equal); Supervision (equal); Writing – review & editing (equal).

DATA AVAILABILITY

The data that support the findings of this study are available from the corresponding authors upon reasonable request.

REFERENCES

- ¹Y. Zhang, Y. Wang, L. Wang, L. Zhu, and Z. Wang, "Highly sensitive photoelectric detection and imaging enhanced by the pyro-phototronic effect based on a photoinduced dynamic Schottky effect in 4H-SiC," *Adv. Mater.* **34**, 2204363 (2022).
- ²Q. Liu, D. Zhou, X. Cai, M. Qi, W. Xu, D. Chen, F. Ren, R. Zhang, Y. Zheng, and H. Lu, "Effect of very high-fluence proton radiation on 6H-SiC photoconductive proton detectors," *IEEE Electron Device Lett.* **40**(12), 1929 (2019).
- ³A. Sciuto, L. Calcagno, S. Di Franco, D. Pellegrino, L. M. Selgi, and G. D'Arrigo, "Radiation hardness of 4H-SiC P-N junction UV photo-detector," *Materials* **15**(1), 264 (2021).
- ⁴M. Bruzzi, "Radiation damage in silicon detectors for high-energy physics experiments," *IEEE Trans. Nucl. Sci.* **48**(4), 960 (2001).
- ⁵H. Amekura, N. Nishimoto, and K. Kono, "Radiation-induced two-step degradation of Si photoconductors and space solar cells," *IEEE Trans. Nucl. Sci.* **45**(3), 1508 (1998).
- ⁶N. Watanabe, T. Kimoto, and J. Suda, "4H-SiC pn photodiodes with temperature-independent photoresponse up to 300 °C," *Appl. Phys. Express* **5**(9), 094101 (2012).
- ⁷S. Hou, P. E. Hellström, C. M. Zetterling, and M. Östling, "550 °C 4H-SiC p-i-n photodiode array with two-layer metallization," *IEEE Electron Device Lett.* **37**(12), 1594 (2016).
- ⁸Z. Fu, M. Zhang, S. Han, J. Cai, R. Hong, X. Chen, D. Lin, S. Wu, Y. Zhang, D. Fu, Z. Wu, B. Zhang, F. Zhang, and R. Zhang, "High-speed and responsivity 4H-SiC 8 × 8 p-i-n ultraviolet photodiode arrays with micro-hole structure," *IEEE Trans. Electron Devices* **70**(8), 4264 (2023).
- ⁹A. Sciuto, F. Roccaforte, S. Di Franco, V. Raineri, S. Billotta, and G. Bonanno, "Photocurrent gain in 4H-SiC interdigit Schottky UV detectors with a thermally grown oxide layer," *Appl. Phys. Lett.* **90**(22), 223507 (2007).
- ¹⁰Y. Xu, D. Zhou, H. Lu, D. Chen, F. Ren, R. Zhang, and Y. Zheng, "High-temperature and reliability performance of 4H-SiC Schottky-barrier photodiodes for UV detection," *J. Vac. Sci. Technol., B* **33**(4), 040602 (2015).
- ¹¹A. Vert, S. Soloviev, J. Fronheiser, and P. Sandvik, "Solar-blind 4H-SiC single-photon avalanche diode operating in Geiger mode," *IEEE Photonics Technol. Lett.* **20**(18), 1587 (2008).
- ¹²X. Zhou, X. Tan, Y. Wang, X. Song, T. Han, J. Li, W. Lu, G. Gu, S. Liang, Y. Lu, and Z. Feng, "High-performance 4H-SiC p-i-n ultraviolet avalanche photodiodes with large active area," *Chin. Opt. Lett.* **17**, 090401 (2019).
- ¹³Y. Bai, C. Z. Li, H. J. Shen, Y. D. Tang, and X. Y. Liu, "Structural optimization of 4H-SiC BJT for ultraviolet detection with high optical gain," *Mater. Sci. Forum* **858**, 1036 (2016).
- ¹⁴Y. Liu, L. Yuan, C. Sun, Y. Zhang, X. Tang, and Y. Zhang, "Three-dimensional design of a 4H-SiC NPN lateral phototransistor for micro-pixel in ultraviolet optoelectronic integration," *IEEE Trans. Electron Devices* **70**(12), 6399 (2023).
- ¹⁵C. Sun, H. Guo, L. Yuan, X. Tang, Y. Zhang, Q. Song, and Y. Zhang, "Analysis of SiC NPN ultraviolet phototransistor under ultrahigh temperature," *IEEE Trans. Electron Devices* **70**(5), 2342 (2023).
- ¹⁶Z. Luo, T. Chen, A. C. Ahyi, A. K. Sutton, B. M. Haugerud, J. D. Cressler, D. C. Sheridan, J. R. Williams, P. W. Marshall, and R. A. Reed, "Proton radiation effects in 4H-SiC diodes and MOS capacitors," *IEEE Trans. Nucl. Sci.* **51**(6), 3748 (2004).
- ¹⁷K. Niskanen, A. Javanainen, C. Martinella, W. Hajdas, U. Grossner, and H. Kettenun, "Proton energy dependence of SiC power MOSFET single-event burnout sensitivity," *IEEE Trans. Nucl. Sci.* **72**(4), 1412 (2025).
- ¹⁸A. C. Ahyi, S. R. Wang, and J. R. Williams, "Gamma irradiation effects on 4H-SiC MOS capacitors and MOSFETs," *Mater. Sci. Forum* **527-529**, 1063 (2006).
- ¹⁹P. Dong, Y. Cui, Z. Chen, Y. Gu, K. Zhou, S. Deng, L. Zhong, Y. Zhang, and J. Li, "Effects of neutron irradiation on the static and switching characteristics of high-voltage 4H-SiC p-type gate turn-off thyristors," *IEEE Trans. Electron Devices* **66**(9), 3910 (2019).
- ²⁰T. Li, X. Tao, W. Xu, D. Zhou, F. Ren, D. Chen, R. Zhang, Y. Zheng, and H. Lu, "Geiger-mode operation 4H-SiC recessed-window avalanche photodiodes fabricated by N ion implantation," *IEEE Photonics Technol. Lett.* **35**(14), 761 (2023).
- ²¹Y. Wang, W. Li, W. Xu, F. Zhou, D. Zhou, F. Ren, D. Chen, R. Zhang, Y. Zheng, and H. Lu, "Reach-through-collector based 4H-SiC phototransistor enabling nW/cm² UV detection," *IEEE Electron Device Lett.* **45**(4), 617 (2024).
- ²²Z. Wang, D. Zhou, W. Xu, Y. Wang, F. Ren, D. Chen, R. Zhang, Y. Zheng, and H. Lu, "4H-SiC δn-i-p extreme ultraviolet detector with gradient doping-induced surface junction," *IEEE Electron Device Lett.* **43**(6), 906 (2022).
- ²³J. Vobecký, P. Hazdra, S. Popelka, and R. K. Sharma, "Impact of electron irradiation on the ON-state characteristics of a 4H-SiC JBS diode," *IEEE Trans. Electron Devices* **62**(6), 1964 (2015).
- ²⁴D. Axen, F. Dallaire, C. David, M. Fincke-Keeler, L. Kurchaninov, R. Keeler, P. Krieger, C. Leroy, R. McPherson, G. Oakham, P. Poffenberger, K. Randrianarivony, Y. H. Shin, I. Trigger, and J. Turner, "Diamond detector irradiation tests at TRIUMF," *J. Inst.* **6**, P05011 (2011).
- ²⁵P. Hazdra and J. Vobecký, "Radiation defects created in n-type 4H-SiC by electron irradiation in the energy range of 1-10 MeV," *Phys. Status Solidi A* **216**, 1900312 (2019).
- ²⁶C. Hemmingsson, N. T. Son, O. Kordina, J. P. Bergman, E. Janzén, J. L. Lindström, S. Savage, and N. Nordell, "Deep level defects in electron-irradiated 4H-SiC epitaxial layers," *J. Appl. Phys.* **81**(9), 6155 (1997).
- ²⁷A. Castaldini, A. Cavallini, L. Rigutti, and F. Nava, "Low temperature annealing of electron irradiation induced defects in 4H-SiC," *Appl. Phys. Lett.* **85**(17), 3780 (2004).
- ²⁸L. Storasta, J. P. Bergman, E. Janzén, A. Henry, and J. Lu, "Deep levels created by low energy electron irradiation in 4H-SiC," *J. Appl. Phys.* **96**(9), 4909 (2004).
- ²⁹I. Capan, T. Brodar, J. Coutinho, T. Ohshima, V. P. Markevich, and A. R. Peaker, "Acceptor levels of the carbon vacancy in 4H-SiC: Combining Laplace deep level transient spectroscopy with density functional modeling," *J. Appl. Phys.* **124**(24), 245701 (2018).
- ³⁰G. Alfieri, E. V. Monakhov, B. G. Svensson, and M. K. Linnarsson, "Annealing behavior between room temperature and 2000 °C of deep level defects in electron-irradiated n-type 4H silicon carbide," *J. Appl. Phys.* **98**(4), 043518 (2005).
- ³¹H. M. Ayedh, R. Nipoti, A. Hallén, and B. G. Svensson, "Elimination of carbon vacancies in 4H-SiC employing thermodynamic equilibrium conditions at moderate temperatures," *Appl. Phys. Lett.* **107**(25), 252102 (2015).